Fig. 1a (partial) — EBSD map and crystallographic triangle. Legend: Austenite (blue square), Ferrite (red triangle), 10 μm scale bar, (001).

austenite is enriched in Ni and N, whereas the ferrite contains more Fe, Cr and Mo. The ferrite and austenite phases exhibit different electrical/electrochemical and magnetic properties, as observed by using Atomic Force Microscopy (AFM)-based techniques [18–22]. However, there is little information about the difference in the passive film formed on the two phases of duplex stainless steels. Chemical analysis of the passive film formed on the individual phases has previously been performed through etching [10], local sputtering [23], and using single-phase materials [9], all of which have led to findings of the passive film thickness and composition. However, the results are less relevant to the naturally formed native passive film on the duplex stainless steel due to the changes of the surface film induced by the sample preparation.

Local characterization, down to the size of single grains, of the passive film is desirable for a comprehensive understanding of the passivity and corrosion resistance of duplex stainless steel. In this work, the variations in chemical composition and thickness of the surface layer over individual austenite and ferrite grains were analyzed by using synchrotron hard X-ray photoemission electron microscopy (HAXPEEM), with a lateral resolution down to 1 μm. This allows the comparison between austenite and ferrite phases and between individual grains. Details of the experimental approach of the HAXPEEM have been reported previously [24]. In this paper, we present a comprehensive local chemical analysis of the native passive film formed on a super duplex stainless steel, on the level of the average, individual phases, and individual grain orientations, based on data from 58 single grains. The results reported in this paper provide new insights into the native passive film of duplex stainless steel, which cannot be obtained with conventional surface analysis techniques.

2. Experimental

2.1. Material and sample preparation

The coupon-shaped specimen was cut along the rolling direction from a 10 mm thick plate of super duplex stainless steel of grade 25Cr-7Ni (UNS S32750), supplied by Sandvik Materials Technology, Sweden. This grade contains 25 % Cr, 7 % Ni, 3.4 % Mo, and 0.3 % N (wt. %) as the main alloying elements (bal. Fe). The dimensions of the specimen were 10 mm × 10 mm × 1 mm. The surface was first wet-ground to 4000-grit with SiC sandpapers, followed by sequential polishing using 3, 1 and ¼ μm diamond paste, and then fine polishing in an active oxide polishing suspension (OPS) to remove the deformation, induced by grinding and polishing, from the surface. A short final re-polishing with ¼ μm diamond paste was done to remove the chemically-altered oxide film formed during the OPS polishing. The specimens were rinsed in MilliQ water and left in ambient conditions for one week before the experiment [24].

2.2. X-ray photoelectron measurements

Prior to the measurements, three fiducial Pt-containing markers with different sizes were hierarchically arranged by electron-beam induced deposition (EBID) on the sample to enable selection the area of interest [25]. The markers facilitated the identification of the same area in the HAXPEEM measurement and the post-analysis with electron backscatter diffraction (EBSD). HAXPEEM is a microscopic surface chemical analysis technique, and details of the measurement procedures have been described previously [24]. In short, the HAXPEEM measurement was conducted with excitation energy of 4 keV at the P22 beamline at PETRA III at DESY (Hamburg, Germany) [26]. The measurement generated photoemission electron images for different elements of the measured area, from which photoelectron spectra of Cr 2p, Fe 2p, Ni 2p and O 1s core levels were obtained. The Mo signals were too weak to be analyzed. A beam size of 70 μm × 10 μm with a field of view of ca. 90 μm × 90 μm were employed for the measurements.

This paper is focused on the analysis of the native passive film of the sample formed in ambient air. A combination of the HAXPEEM and EBSD images of the analyzed surface area enabled identification of individual grains and their crystallographic orientations. Here, crystallographic orientation (hkl) is referred to the crystal face parallel to the sample surface, since a rotation around a normal [hkl] to this surface is not expected to influence the oxidation behavior so a complete orientation description is not necessary. The individual grains yielded an acceptable signal/noise ratio, so X-ray photoelectron spectroscopy (XPS) spectra from each individual grain could be extracted from the HAXPEEM data. Within the measured surface area, 22 austenitic grains (no.1–22) and 36 ferritic grains (no. 23-58) were analyzed, with a total area of ca 430 μm² and 2072 μm² for the austenite and ferrite, respectively. All analyzed grains are numbered in Fig. 1a, and their crystallographic orientations are shown in the crystallographic triangle given in Fig. 1b.

The HAXPEEM provides microscopic images of the photoelectron intensity from which XPS spectra from individual grains can be extracted. However, the HAXPEEM data have a low energy resolution, and the XPS spectra from small areas suffer from weak signals, which give a low signal-to-noise ratio and thus make the spectra deconvolution difficult from a single grain. Complementary hard X-ray photoelectron spectroscopy (HAXPES) measurements of the same sample surface were performed at the same beamline. The HAXPES data have a high signal-to-noise ratio, which served as a reliable reference for peak assignment in the analysis of the HAXPEEM data. The detailed HAXPES results and analysis will be reported elsewhere, while an overview HAXPES survey spectra is shown in Figure S1 in the supplementary material.

3.1. Analysis of individual g...

In this work, the XPS spectra of Cr, Fe, Ni, O elem... tracted from the HAXPEEM data of the individual grains. By summing up the signals from the grains of the same orientation, the same phase, and all the grains, the summed XPS spectra representing each grain orientation, each individual phase, and the material (all the grains) were obtained and analyzed. The results from fitting of XPS spectra of individual grains were used to evaluate the thickness and composition of the major components of local passive films formed on the individual grains [24]. Then, the average thickness and composition of the passive film on each crystallographic orientation of each phase were obtained through deconvolution of the summed XPS spectra from the grains of the same orientation and the same phase. Similarly, the average thickness and composition of the austenite and ferrite, respectively, were obtained by fitting the summed XPS spectra from all the grains belonging to the same phase. The summation of the signals increases the signal-to-noise ratio; however, the averaging may hide variations between individual grains and between different crystallographic orientations. The standard deviation was calculated from all the grains included in the average, for the particular phase, and each grain orientation.

3.2. Deconvolution of XPS spectra

The spectra deconvolution was performed by using Casa XPS software (version 2.3) on the raw data without any normalization. The spectra were background-subtracted using a Shirley background, and then normalized to the strongest peak to facilitate comparison. The binding energies of the HAXPES measurement were calibrated by the Fermi level of a gold foil and the carbon peak of $-CH-CH-$ fixed at 284.8 eV [27]. The binding energies of the HAXPEEM spectra were calibrated with Fe 2p metal peak according to the HAXPES spectra.

The O 1s spectra could be deconvoluted into O^{2-} and OH^- components, indicating the presence of oxides and hydroxides in the native passive film. Following the literature, the metallic components (Cr_{met}, Fe_{met}, Ni_{met}) were fitted with a Lorentzian asymmetric peak shape [28], and the remaining components were fitted with symmetric Lorentzian/Gaussian peak shape with a ratio of 70/30 [13]. The XPS spectra of Cr were satisfactorily fitted by using the metallic Cr and the oxidic components Cr_2O_3 and $Cr(OH)_3$ [29]. Regarding oxidic Fe components, both Fe^{2+} and Fe^{3+} may co-exist in the oxide and hydroxide forms, and in addition Fe_3O_4 is also possible [29]. The total signal of oxidized Fe was ca 10 % of the metal peak, and hence too low for making unambiguous peak assignment of many oxidic components. For simplicity, the Fe $2p_{3/2}$ spectra were fitted with only Fe_{met}, Fe^{2+} oxide, and Fe^{3+} oxyhydroxide components. Although deconvolution of Fe spectra into more components have been reported [29], in this work, no such effort was made considering the weak signals and lack of certainty for the peak assignment. Moreover, the Ni $2p_{3/2}$ spectra from the HAXPEEM show that Ni is mainly in its metallic form. The small peak at higher binding energy may indicate a minor amount of Ni oxide as reported in literature [30]. However, it may also be the satellite peak of metallic Ni [31,32], and was thus ignored due to lack of certainty.

The summed spectra of all grains and of each phase had high signal-to-noise ratio, and the deconvolution of these spectra yielded the peak position, i.e., the binding energy (BE), and the full width at half maximum (FWHM) for the components, see Table 1. These parameters were then used in the spectra fitting of the individual grains and each crystallographic orientation. In the fitting procedure, the BE and FWHM were allowed to vary slightly (± 0.2 eV) considering the disparity of the spectral resolution of the techniques [29,33].
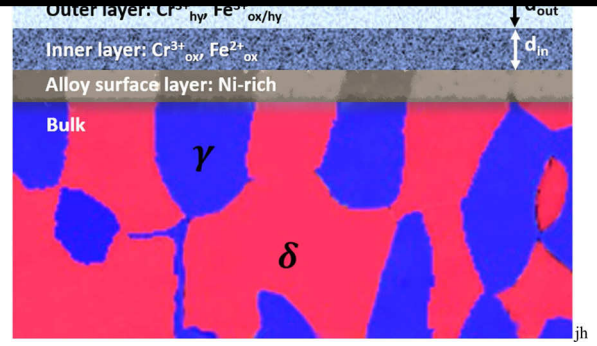

Fig. 2. Simplified two-layer model of the native passive film: an inner layer composed of Cr^{3+} and Fe^{2+} oxides and the outer layer composed of Cr^{3+} hydroxide and Fe^{3+} oxyhydroxide. The model was used for estimating thickness of the oxide and hydroxide layers and the contents of the major components. The presence of a Ni-enriched alloy surface layer beneath the passive film is also shown. For the bulk, the two phases are represented as red ferrite (δ) and blue austenite (γ).

3.3. Information depth and model of the passive film

The information depth of the emanating signals from the probed surface was calculated according to Eqs. (1) and (2), and considering the bulk composition of the alloy (stainless steel):

$$d = 3\lambda_{Alloy}\sin(\theta) \tag{1}$$

$$\lambda_{Alloy} = (x^{Fe}_{Alloy}\lambda^{Fe}_{hv} + x^{Cr}_{Alloy}\lambda^{Cr}_{hv}...+x^{j}_{Alloy}\lambda^{j}_{hv}) \tag{2}$$

where d is the information depth; λ the inelastic mean free path of photoelectrons for an individual element, λ^{j}_{hv}, and for the alloy, λ_{Alloy} ; θ the take-off angle of excited electrons; x the atomic percentage of the element j in the alloy; hv the beam energy. The atomic percent of each element in the alloy and calculated λ^{j}_{hv} of the element used for the calculation of λ_{Alloy} are given in Table S1 in the supplementary material. The X-ray beam energy of 4 keV and the take-off angles of 90° give an information depth of 15 nm for the HAXPEEM measurement.

The native passive film on stainless steel is formed as a result of oxidation reactions of the metal elements present in the material. The elemental oxygen affinities and oxidation rates determine the composition and thickness of the oxide film [1,34]. The passive film formed on stainless steels has been reported to have a two-layer structure, i.e., an oxide inner layer and a hydroxide outer layer [35]. In our study, additional HAXPEEM measurements were performed at an excitation energy of 6 keV, and the results (Figure S2 in the supplementary material) show that the signal intensity of the hydroxide decreased more than that of the oxide at the higher excitation energy (less surface sensitive), which supports the two-layer model. Fig. 2 shows schematically the two-layer model, where the inner layer refers to Cr^{3+} and Fe^{2+} oxides with a thickness of d_{in}, and the outer layer refers to Cr^{3+}
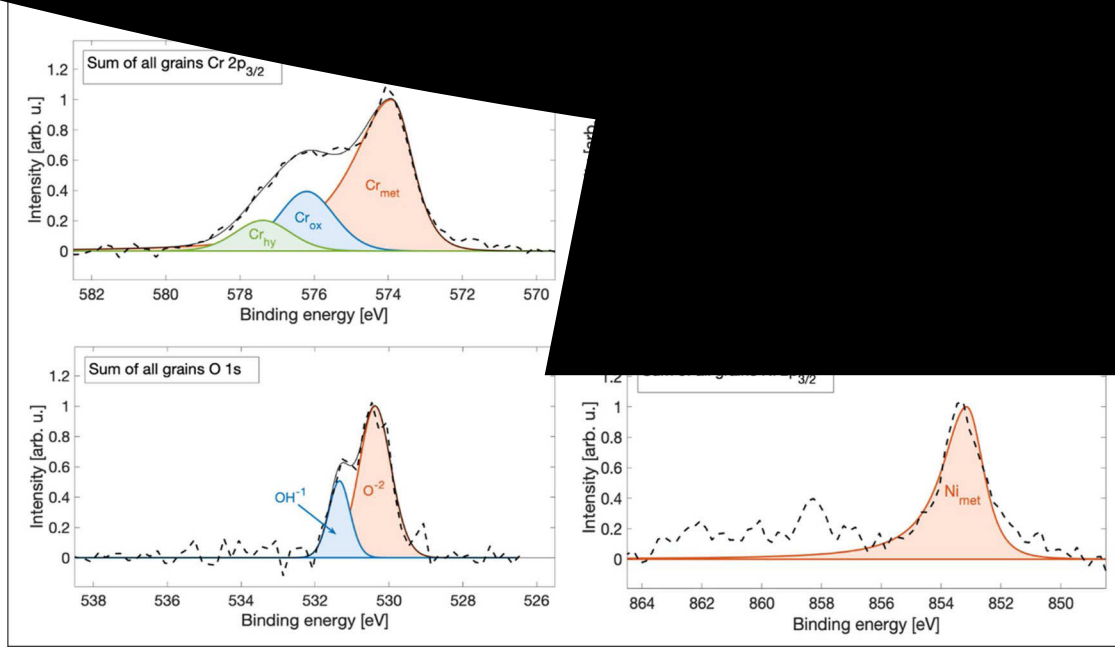
Fig. 3. Summed XPS spectra extracted from the HAXPEEM data from all the 58 analyzed grains and the deconvolution components for Cr 2p$_{3/2}$, Fe 2p$_{3/2}$, O 1s and Ni 2p$_{3/2}$. The spectra are normalized (to the strongest leak) for easy comparison.

Table 2
Thickness and Cr content of the inner and outer layers of the native passive film obtained from the summed spectra of all analyzed grains, and the mean values of all individual grains.

	Summed spectra		Mean of all individual grains	
	Thickness (nm)	Cr content (at %)	Thickness (nm)	Cr content (at %)
Inner layer	1.4	75	1.2 (± 0.3)	67 (± 16)
Outer layer	0.9	88	0.9 (± 0.3)	75 (± 14)
Total/average	2.3	81	2.1 (± 0.4)	71 (± 10)

Values in the parentheses are standard derivations among all analyzed grains.

hydroxide and Fe^{3+} oxyhydroxide with the thickness of d_{out}.

In this simplified model, a possible minor amount of Fe^{3+} oxide is included in the hydroxide layer, so the outer layer can also be regarded as the oxyhydroxide layer. The existence of a minor amount of oxidative Mo-species in the passive film is neglected in the quantitative analysis. Preferential oxidation of Cr and Fe forming the surface oxides leads to a modified alloy layer beneath the passive film, which is enriched in Ni and depleted in Cr and Fe [1]. The so-called alloy surface layer is also illustrated in Fig. 2. In our previous work, this layer was found to have a higher density than the bulk material [36]. The composition and thickness of the alloy surface layer have been measured and estimated by other investigators [13–15,37]. A detailed discussion of the alloy surface layer requires data of Mo species, which are not available in the HAXPEEM results, and is therefore not included in this paper.

3.4. Calculation of thickness and Cr content

The two-layer model of the native passive film in Fig. 2 was used to estimate the thickness and Cr content of the inner and outer layers. Using the intensity data of the metallic and oxidic components of Fe and Cr, the thickness and Cr content of the inner layer and outer layer were calculated using the following equations [9,13,38]:

$$d_{in} = \lambda_j^{in}\sin(\theta) \cdot \ln\left(1 + \frac{I_j^{in} D_j^{met} \lambda_j^{met}}{I_j^{met} D_j^{in} \lambda_j^{in}}\right) \tag{3}$$

$$d_{out} = \lambda_j^{out}\sin(\theta) \cdot \ln\left(1 + \frac{I_j^{out} D_j^{in} \lambda_j^{in}}{I_j^{in} D_j^{out} \lambda_j^{out}}\right) \cdot \left(1 - EXP\left(-\frac{d_{in}}{\lambda_j^{in} Sin(\theta)}\right)\right) \tag{4}$$

Where d is the thickness of the single-layer; λ the inelastic mean free path and θ the take-off angle of excited electrons; I the peak intensity; D_j is the component concentration defined as $D_j = \frac{\rho_j}{M_j} \cdot x_j$, where ρ is the volume density, M the molar mass, x the atomic percentage of the component j (only Cr and Fe were considered here). The subscript and superscript of 'in', 'out', and 'met' refer to the inner layer, outer layer, and the metallic components, respectively. These equations are derived based on the factors that influence the peak intensity of photoelectrons emitted from the bulk and the oxidic layers, respectively. Photoelectrons emitted from the oxidic layers have deviating inelastic mean free path and thickness dependence than those emitted from the bulk [39]. Most parameters in Eq.s (3) and (4) are constants, while the thickness d and the composition x are unknowns for the oxide and hydroxide layers. By solving the Eq.s (3) and (4) for Cr and Fe, the thickness and Cr content can be obtained, which is further explained in the supplementary material. Because the native passive film is assumed to consist of Cr and Fe components only, the results from this work may slightly differ from other studies considering all oxidic Cr, Fe, and a minor amount of Mo components. Our focus is the evaluation of the lateral distribution of the major components of Cr and Fe.

3.5. Global analysis by HAXPEEM

Fig. 3 displays the summed XPS spectra of Cr 2p$_{3/2}$, Fe 2p$_{3/2}$, Ni 2p$_{3/2}$, and O1 s from all the analyzed grains and the components used for spectra deconvolution. Following the two-layer model in Fig. 2, the thickness and Cr content of the inner and outer layers of the native passive film were calculated according to Eqs (3) and (4), and the results are shown in Table 2. This global approach gives the overall average values since the analyzed area contains both austenite and
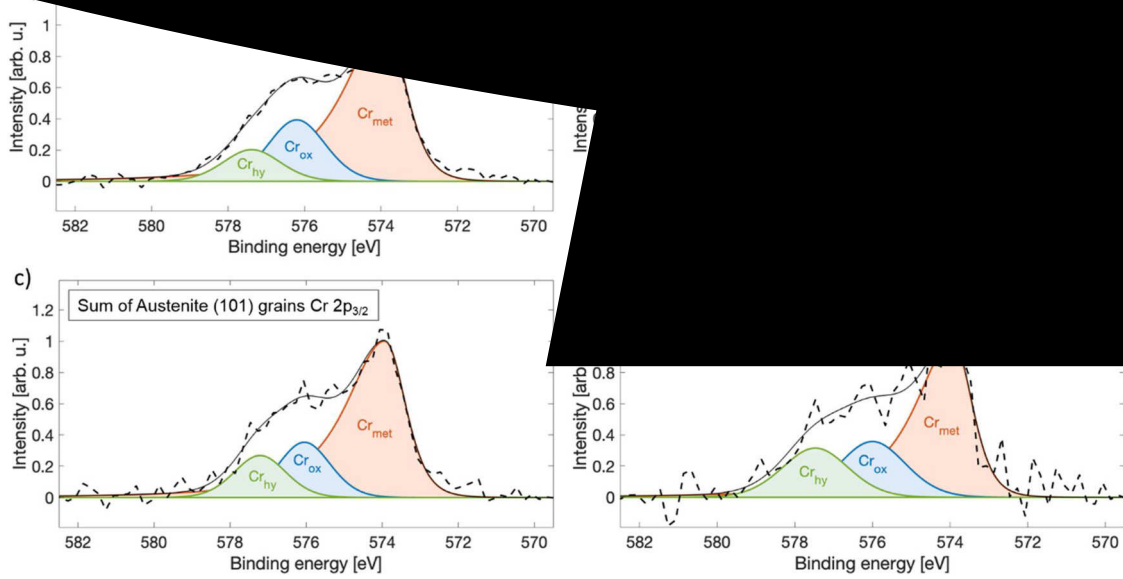
Fig. 4. Normalized XPS spectra of Cr $2p_{3/2}$ extracted from the HAXPEEM data: (a) summed spectrum of all analyzed grains, (b) summed spectrum of all austenite grains, (c) summed spectrum of all austenite grains with (101) orientation, (d) spectrum of one single austenite grain with (101) orientation.
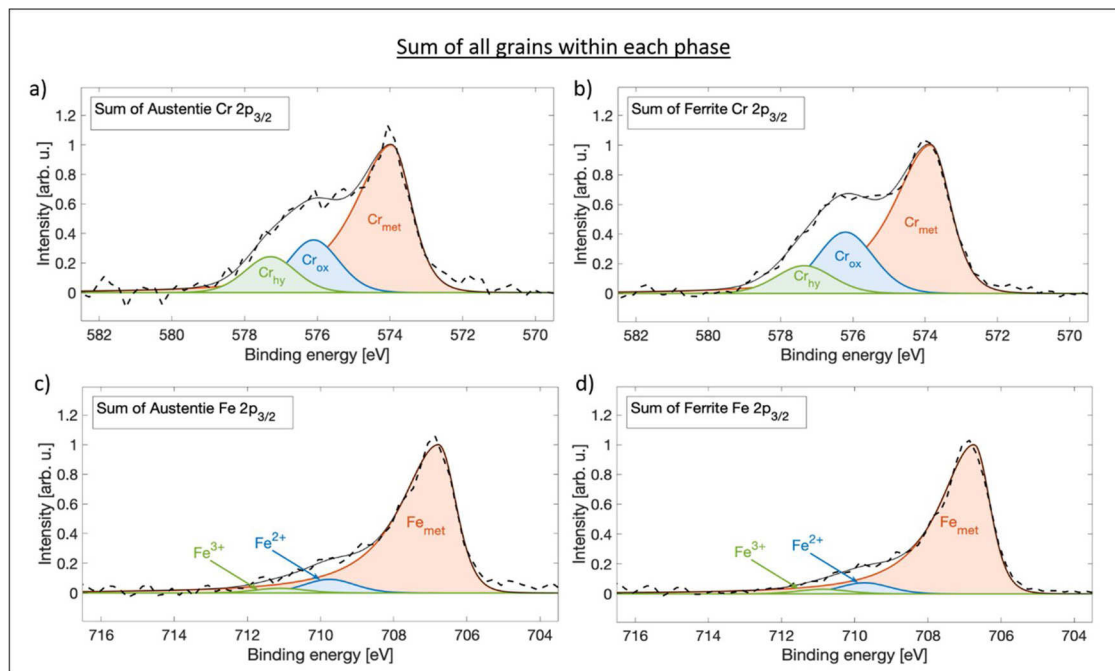

Fig. 5. Summed XPS spectra of Cr $2p_{3/2}$ (a, b) and Fe $2p_{3/2}$ (c, d) of all analyzed austenite (a, c) and ferrite (b, d) grains, and the deconvolution components. The spectra are normalized to the same scale.

ferrite grains. Based on this analysis, the thickness was 1.4 nm for the inner layer and 0.9 nm for the outer layer. In the native passive film (only considering Cr and Fe components), the Cr content was 75 at% in the inner layer and 88 at% in the outer layer.

In a mean average approach, the spectra from individual grains were fitted, and the mean values of the thickness and Cr content were calculated, which are also given in Table 2 for comparison. Because of weak signals for individual grains, the spectra fitting may give relatively larger errors of the data obtained from the mean average approach.

The analysis of the summed spectra gave a total thickness of 2.3 nm for the native passive film, which is consistent with the result of the

mean value, 2.1(± 0.4), obtained from mean average of all individual grains. This is in general agreement with the reported thickness for passive films formed on stainless steels [2]. Moreover, the global average Cr content in the native passive film was measured as ca. 80 at % (data from the summed spectra), which is also in line with common observations that Cr is the dominant component in passive films of stainless steels [2,13,14]. These results validate the HAXPEEM for quantitative analysis of the passive films.

3.6. Local analysis of the HAXPEEM data

The HAXPEEM data are used for analysis of lateral variations in the

	Thickness (nm)					
	Inner layer	Outer layer	Total			
Austenite	1.0	0.8	1.8			
Ferrite	1.0	0.6	1.6			
	Thickness (nm)					
	Inner layer	Outer layer	Total			
Austenite	1.2 (± 0.4)	0.9 (± 0.3)	2.1 (			
Ferrite	1.2 (± 0.3)	0.9 (± 0.2)	2.1 (± 0.4)	70 (± 15)	77 (± 13)	73 (± 9)

Values in parentheses are standard derivations among all grains of the single phase.
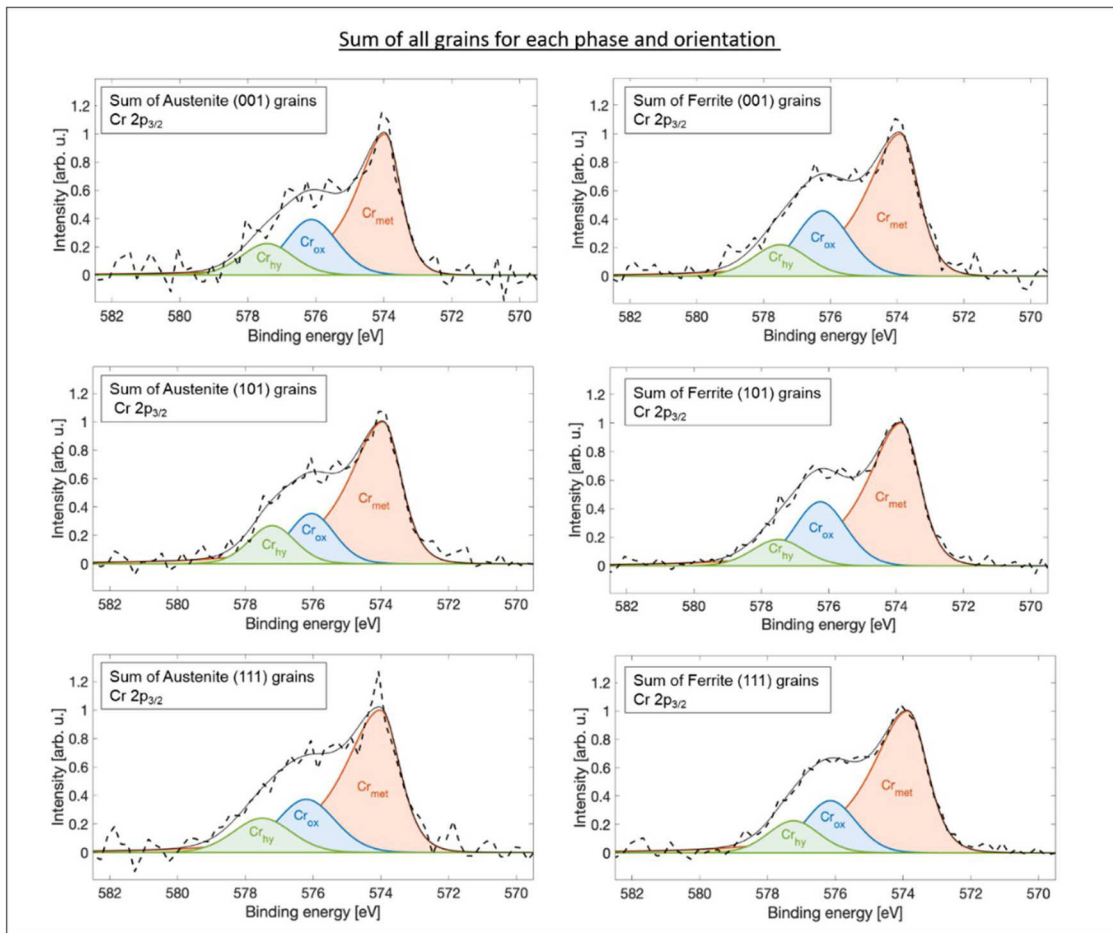

Fig. 6. Summed spectra of Cr 2p$_{3/2}$ from the grains of each orientation for austenite and ferrite, respectively, and the deconvolution components. The spectra are normalized to the same scale.

thickness and Cr content of the native passive film formed on the super duplex stainless steel. In addition to the XPS spectra from the individual grains, the summed spectra representing each crystallographic orientation, and each phase, were also generated for spectra fitting. As an example, Fig. 4 shows the Cr spectra obtained from the entire analyzed area, all the austenite grains, all the austenite grains with (101) orientation, and one austenite grain with (101) orientation, respectively. The signal-to-noise ratio increases with increasing number of grains, so a larger analyzed area yields an improved quality of fitting. From a statistics point of view, when averaging, the data from individual grains

of a specific group give a standard deviation among the grains of that group. Similarly, the standard deviation for a specific orientation of a specific phase represents the difference among the grains of that particular group, as exemplified in Table 2. In the following sections, results from fitting of both the summed spectra and of the individual grains (with the mean and standard deviation values) are included for discussion about the differences between the two phases, and between the crystallographic orientations.

Tab...
Thickness (nm)...
grains of each orientation of ...
and spectra of individual grains.

	Summed spectra			Mean of individual grains		
	Inner layer	Outer layer	Total	Inner layer	Outer layer	Total
Austenite						
(001)	1.3	1.1	2.4	1.2 (± 0.4)	1.2 (± 0.1)	2.4 (± 0.4)
(101)	1.2	1.0	2.2	1.2 (± 0.4)	0.8 (± 0.3)	1.9 (± 0.4)
(111)	1.2	1.0	2.2	1.4 (± 0.3)	1.2 (± 0.3)	2.6 (± 0.4)
Ferrite						
(001)	1.3	0.8	2.1	1.2 (± 0.4)	0.9 (± 0.1)	2.1 (± 0.5)
(101)	1.2	0.7	1.9	1.3 (± 0.3)	0.9 (± 0.2)	2.2 (± 0.3)
(111)	1.1	0.8	1.9	1.2 (± 0.2)	0.8 (± 0.2)	2.0 (± 0.3)

Values in parenthesis are standard deviation among the individual grains.

3.6.1. The passive film on austenite and ferrite phases

Deconvolution of the summed spectra of Cr $2p_{3/2}$ and Fe $2p_{3/2}$ of the austenite and ferrite phases were done, as shown in Fig. 5, using the parameters given in Table 1. The signal intensity was high for oxidative Cr components, but low for oxidative Fe components. Based on the fitting results, the thickness and Cr content of the oxide and hydroxide layers were calculated for the austenite and ferrite, respectively, as shown in Table 3. For visual comparison, the data from averaging of individual grains are also presented in a graphical manner with a box plot as exemplified in Figure S3 in the supplementary material, which displays the mean and median values as well as scattering of data (standard derivation bars) for the Cr content of the inner layer, outer layer, and average of the whole native passive film, respectively. The box plot is helpful for a more detailed statistical analysis of the significance of the observed differences.

There are small differences in the thickness and Cr content values obtained from the summed spectra and those from averaging of individual grains, which are due to different errors in the two ways of analysis. Nevertheless, the two sets of data show same trends (Table 3). The outer hydroxide layer is thinner but has a higher Cr content than the inner oxide layer. The Cr content of the oxide layer is slightly higher on the ferrite than on the austenite. The homogeneity of the passive film formed on the two phases of duplex stainless steel has been a question of debate [9]. The synchrotron HAXPEEM measurement provided the possibility to directly measure the lateral variations in the thickness and the Cr content of the passive film. The thickness of both the inner layer and outer layer is similar between the two phases under the assumptions used in the calculation. The higher Cr content in the oxide layer on the ferrite can be explained by the higher Cr content in the ferrite, since the surface oxide was formed due to oxidation reaction.

that, for the different grain orientations the thickness varies from 1.1 to 1.3 nm for the inner layer and from 0.7 to 1.1 nm for the outer layer. The ferrite grains seem to have a slightly thinner outer layer compared to the austenite grains. For both austenite and ferrite grains, the (001) orientation seems to have a slightly thicker native passive film (data from summed spectra).

Table 5 gives the Cr content of the inner and outer layers of the native passive film for different grain orientations of each phase, calculated from the summed spectra and the spectra of individual grains, respectively. A box plot graphically showing the mean, median, and scattering of the Cr content data from the individual grains can be found in the supplementary material (Figure S5). The results show that the average Cr content of the native passive film is generally higher on the ferrite grains compared to the austenite grains except the (111) orientation, which is similar for the two phases. The passive film (especially the outer layer) on the ferrite grains of (111) orientation seems to have a lower Cr content compared to the ferrite grains of other orientations. However, the Cr content in the passive film is rather uniform for the austenite grains (the difference is not significant between the orientations). The results indicate that the grain orientation has a small but detectable influence on the formation of the native passive film.

A thinner outer (oxyhydroxide) layer of the passive film on the ferrite phase as compared to austenite grains may explain the preferential dissolution of the ferrite phase observed previously [40,41]. Furthermore, a lower Cr content in the passive film on the ferrite grains of (111) orientation could be the reason why the ferrite (111) grains are the most corrosion prone grains as reported in literature [42].

Elemental diffusion coefficients are known to be different for the ferrite and austenite phases of duplex stainless steel. At ambient temperature, the diffusion coefficient (cm^2/s) of Cr is 10^{-42} in ferrite and 10^{-37} in austenite, and for Fe it is 10^{-46} in ferrite and 10^{-53} in austenite [43]. Although the bulk diffusion is very slow, Cr diffuses much faster than Fe, which has an influence on the formation of the passive film (a few nanometers thick), as evidenced by a much higher Cr content in the

Table 5

Cr content (at%) of the inner and outer layers of the native passive film on the grains of each orientation of the same phase, obtained from the summed spectra and spectra of individual grains.

	Nr. of grains	Summed spectra			Mean of individual grains		
		Inner layer	Outer layer	Average	Inner layer	Outer layer	Average
Austenite							
(001)	3	74	67	70	57 (± 28)	63 (± 5)	60 (± 16)
(101)	13	66	73	70	60 (± 15)	72 (± 15)	66 (± 9)
(111)	6	66	73	70	67 (± 17)	76 (± 14)	72 (± 6)
Ferrite							
(001)	6	76	90	83	61 (± 24)	84 (± 6)	73 (± 12)
(101)	11	76	85	81	73 (± 13)	80 (± 12)	76 (± 9)
(111)	19	65	76	71	71 (± 12)	73 (± 15)	72 (± 9)

Values in parenthesis are standard deviation among the individual grains.

pass[...]

content of the [...]

higher Cr content in the fer[...]

Regarding the influence of grain ori[...] there is no diffusion anisotropy for cubic crystal systems, [...] difference among the different orientations. Hence, the orientation-dependent effect is likely associated with the difference in surface reactivity rather than bulk diffusion. On the other hand, diffusion within the surface oxide may have an influence on the passive film growth. In a study of oxide growth on the surfaces of BCC Fe crystals, the oxygen diffusion coefficient and activation energy for oxidation differentiate for the crystallographic orientations [44]. Thin oxide film formation on metal surface at ambient temperature has been explained by a high-field theory based on electron tunneling and ion migration though the oxide film under an established electrical field [45]. Point defect model has been developed to describe the formation and degradation of passive films on metal surfaces, taking into account vacancy formation and annihilation, and ionic migration across the passive film [46,47]. For duplex stainless steels containing multiple elements and multiple phases, the oxide formation is very complex and further efforts are needed to understand the formation of passive film and the influence of the grain orientation.

The HAXPEEM measurements presented in this investigation paves the way for future studies of complex materials such as advanced alloys. In particular, the approach is useful to study chemical phenomena with lateral variations on the micron scale, such as phase transformations, grain boundary segregation, and the fate of the passive film upon heating.

4. Conclusions

Global and local analysis of native passive film formed on a 25Cr-7Ni super duplex stainless steel by synchrotron-based HAXPEEM measurements have led to the following conclusions (Mo is disregarded):

- The native passive film has a two-layer feature, with the inner layer dominated by oxides and outer layer by oxyhydroxides, mainly of Cr and Fe. The thickness of the inner layer is 1.4 nm and the outer layer 0.9 nm, thus a total thickness of 2.3 nm for the passive film. When only Cr and Fe are considered, the average Cr content is ca. 80 at%, while the outer layer has a higher content than the inner layer.

- HAXPEEM enables local analysis of passive film formed on individual grains, allowing assessment of the difference between the austenite and ferrite phases, as well as the influence of grain orientation on the passive film.

- There are certain differences in Cr content although the thickness is similar for the passive film between the austenite and ferrite phases. The oxide layer on the ferrite has a higher Cr content, due to the higher content of Cr in the ferrite.

- On the grain level, the thickness of the oxide layer is rather uniform whereas it varies significantly for the oxyhydroxide layer. The grain orientation is observed to have a small but detectable influence on the Cr content in the outer layer of the passive film. On the ferrite grains of (111) orientation, the native passive film, especially in the outer layer, contain a lower Cr content compared to that on other ferrite grains.

Author statement

M.L (Långberg) and F.Z. conducted the experiments, analyzed the data, and wrote the manuscript. E.G. and J.C. conducted the experiments, analyzed the data, and contributed to the preparation of the manuscript. C.Ö. conducted the experiments and contributed to the preparation of the manuscript. M.L (Liu) conducted the experiments and joined the discussion. C.W. and A.G. prepared the synchrotron HAXPEEM experimental setup and helped the experiments. C.S. prepared the synchrotron HAXPES experimental setup and helped the

The authors declare that they have no known competing financial interests or personal relationships that could have appeared to influence the work reported in this paper.

Appendix A. Supplementary data

Supplementary material related to this article can be found, in the online version, at doi:https://doi.org/10.1016/j.corsci.2020.108841.

References

[1] Chap. 3-6, in: P. Marcus (Ed.), in Corrosion Mechanisms in Theory and Practice, CRC Press, Taylor and Francis, 2011.
[2] C.O.A. Olsson, D. Landolt, Passive films on stainless steels—chemistry, structure and growth, Electrochim. Acta 48 (9) (2003) 1093–1104.
[3] P. Marcus, V. Maurice, Passivity of metals and alloys, in: P. Marcus (Ed.), Materials Science and Technology, Wiley-VCH Verlag GmbH & Co. KGaA, 2006.
[4] V. Maurice, P. Marcus, Progress in corrosion science at atomic and nanometric scales, Prog. Mater. Sci. 95 (2018) 132–171.
[5] P. Schmuki, From Bacon to barriers: a review on the passivity of metals and alloys, J. Solid State Electrochem. 6 (2002) 145–164.
[6] K. Lutton, et al., Understanding multi-element alloy passivation in acidic solutions using operando methods, Electrochem. Commun. 80 (2017) 44–47.
[7] D.D. Macdonald, On the tenuous nature of passivity and its role in the isolation of HLNW, J. Nucl. Mater. 379 (1–3) (2008) 24–32.
[8] E. Tcharkhtchi-Gillard, et al., Kinetics of the oxidation of stainless steel in hot and concentrated nitric acid in the passive and transpassive domains, Corros. Sci. 107 (2016) 182–192.
[9] E. Gardin, et al., Comparative study of the surface oxide films on lean duplex and corroponding single phase stainless steel by XPS and ToF-SIMS, Corros. Sci. 143 (2018) 403–413.
[10] Y. Wang, X. Cheng, X. Li, Electrochemical behavior and compositions of passive films formed on the constituent phases of duplex stainless steel without coupling, Electrochem. Commun. 57 (2015) 56–60.
[11] V. Vignal, et al., Influence of the passive film properties and residual stresses on the micro-electrochemical behavior of duplex stainless steels, Electrochim. Acta 55 (23) (2010) 7118–7125.
[12] H.-H. Strehblow, Passivity of metals studied by surface analytical methods, a review, Electrochim. Acta 212 (2016) 630–648.
[13] Z. Wang, et al., Passivation-induced physicochemical alterations of the native

(2019) C...

[14] V. Maurice, et al., E... phology of passivated austenitic ... (2015) 151–170.

[15] B. Zhang, et al., Unmasking chloride attack on the passive fi... Commun. 9 (2559) (2018) 1–9.

[16] X. Zhang, D.W. Shoesmith, Influence of temperature on passive film properties on Ni–Cr–Mo Alloy C-2000, Corros. Sci. 76 (2013) 424–431.

[17] J.-O. Nilsson, Super duplex stainless steels, Mater. Sci. Technol. 8 (8) (1992) 685–700.

[18] M. Femenia, et al., In-situ study of selective dissolution of duplex stainless steel 2205 by electrochemical scanning tunneling microscopy, Corros. Sci. 43 (1939) (2001) 1939–1951.

[19] M. Femenia, J. Pan, C. Leygraf, In-situ local dissolution of duplex stainless steels in 1M H2SO4 + 1M NaCl by electrochemical scanning tunneling microscopy, J. Electrochem. Soc. 149 (2002) B187.

[20] T. Souier, et al., Local electrical characteristics of passive films formed on stainless steel surfaces by current sensing atomic force microscopy, Appl. Surf. Sci. 256 (2010) 2434–2439.

[21] E. Bettini, et al., Influence of grain boundaries on dissolution behavior of a bio-medical CoCrMo alloy: in-situ electrochemical-optical, AFM and SEM/TEM studies, J. Electrochem. Soc. 159 (9) (2012) C422–C427.

[22] N. Sathirachinda, et al., Characterization of phases in duplex stainless steel by magnetic force microscopy/scanning Kelvin probe force microscopy, Electrochem. Solid-State Lett. 11 (2008) C42–C45.

[23] V. Vignal, et al., Passive properties of lean duplex stainless steels after long-term ageing in air studied using EBSD, AES, XPS and local electrochemical impedance spectroscopy, Corros. Sci. 67 (2013) 109–117.

[24] M. Långberg, et al., Characterization of native oxide and passive film on Austenite/Ferrite phases of duplex stainless steel using synchrotron HAXPEEM, J. Electrochem. Soc. 166 (11) (2019) C3336–C3340.

[25] A. Stierle, et al., DESY NanoLab, J. Large-Scale Res. Facil. Jlsrf 2 (A76) (2016) 1–9.

[26] C. Schlueter, et al., The new dedicated HAXPES beamline P22 at PETRAIII, 13th International Conference on Synchrotron Radiation Instrumentation, SRI2018, AIP Conference Proceedings, Taipei, Taiwan, 2019.

[27] T.L. Barr, S. Seal, Nature of the use of adventitious carbon as a binding energy standard, J. Vac. Sci. Technol. A 13 (3) (1995) 1239.

[28] M.C. Biesinger, et al., Resolving surface chemical states in XPS analysis of first row transition metals, oxides and hydroxides: Cr, Mn, Fe, Co and Ni, Appl. Surf. Sci. 257 (2011) 2717.

[29] W. Fredriksson, et al., Full depth profile of passive films on 316L stainless steel based on high resolution HAXPES in combination with ARXPS, Appl. Surf. Sci. 258 (15) (2012) 5790–5797.

[37] C.-O.A. Olsson, et al., Quantifying the metal nickel enrichment on stainless steel, Electrochem. Solid-State Lett. 14 (1) (2011) C1–C3.

[38] I. Frateur, et al., Adsorption of BSA on passivated chromium studied by flow cell EQCM and XPS, Electrochim. Acta 52 (27) (2007) 7660–7669.

[39] C.O.A. Olsson, D. Landolt, Atmospheric oxidation of a Nb–Zr alloy studied with XPS, Corrorsion science 46 (2004) 213–224.

[40] E. Bettini, et al., Study of corrosion behavior of a 2507 super duplex stainless steel: influence of quenched-in and isothermal nitrides, Int. J. Electrochem. Sci. 9 (1) (2014) 61–80.

[41] E. Bettini, et al., Study of corrosion behavior of a 22% Cr duplex stainless steel: influence of nano-sized chromium nitrides and exposure temperature, Electrochim. Acta 113 (2013) 280–289.

[42] J. Fu, et al., Effect of crystallographic orientations on the corrosion resistance of Fe-17Cr ferritic stainless steel, J. Electroanal. Chem. 841 (2019) 56–62.

[43] E. Folkhard, Significance of constitution diagrams for the understanding of welding phenomena, in: E. Folkhard (Ed.), Welding Metallurgy of Stainless Steels, 1988, p. 50.

[44] B. Jeon, et al., Nanoscale oxidation and complex oxide growth on single crystal iron surfaces and external electric field effects, Phys. Chem. Chem. Phys. 15 (2013) 1821–1830.

[45] N. Cabrera, N.F. Mott, Theory of the oxidation of metals, Rep. Prog. Phys. 12 (163) (1949) 163–184.

[46] D.D. Macdonald, The history of the point defect model for the passive state: a brief review of film growth aspects, Electrochim. Acta 56 (4) (2011) 1761–1772.

[47] D.D. Macdonald, Passivity: enabler of our metals based civilisation, Corros. Eng. Sci. Technol. 49 (2) (2014) 143–155.